Dipole-Dependent Waveguiding in an Anisotropic Metal−Organic Framework

Ruomeng Wan, David Mankus,[⊥] Woo Seok Lee,[⊥] Abigail K. R. Lytton-Jean, William A. Tisdale,* and Mircea Dincă*

Read Online

ACCESS | Metrics & More | Article Recommendations | Supporting Information

ABSTRACT: The interaction between excitons and photons underlies a range of emergent technologies, such as directional light emission, molecular lasers, photonic circuits, and polaritonic devices. Two of the key parameters that impact exciton−photon coupling are the binding energy of excitons and the relative orientations between the exciton dipole and photon field. Tightly bound excitons are typically found in molecular crystals, where nevertheless the angular relationship of excitons with photon fields is difficult to control. Here, we demonstrate directional exciton dipoles and photon fields, anchored by metal−ligand coordination. In a pyrene−porphyrin bichromophoric metal−organic framework (MOF), we observe that the perpendicular arrangement of the pyrene- and porphyrin-based exciton dipoles engenders orthogonal polarizations of their respective emissions. The alignment of the directional exciton and photon fields gives rise to an anisotropic waveguide effect, where the pyrene- and the porphyrin-based emissions show distinct spatial distribution within microplate-shaped MOF crystals. This capability to simultaneously host heterogenous excitonic states and anisotropic photon fields points toward MOFs' yet-to-be-realized potential as a platform for advancing the frontier in the field of exciton−photonics, which centers around engineering emergent properties from the interplay between excitons and photons.
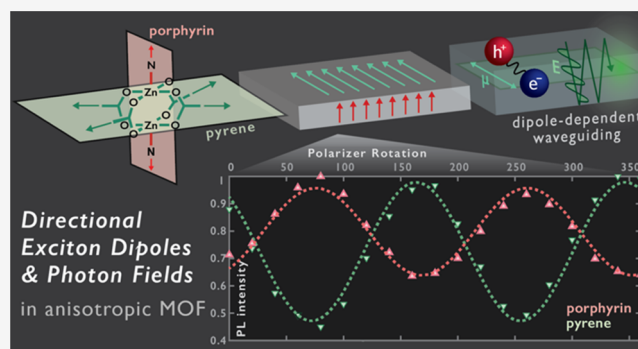
INTRODUCTION

The interaction between the optical transition of a material with the electromagnetic oscillation carries both fundamental and technological significance.[1] It lies at the center of the emerging field of exciton−photonics, which aims to engineer emergent properties by resonantly coupling photons with excitonic materials. In particular, the Frenkel-type excitons typical of organic molecular materials have gained increasing attention because their strong binding energy favors exciton−photon interactions[2] at room temperature.[3] The design of (Frenkel) exciton−photon coupling systems traditionally involved sandwiching molecular organic emitters between extrinsic reflecting surfaces (such as distributed Bragg reflectors).[4−8] More recent progress revealed that light can be reflected by crystal facets themselves, which act as inherent microresonators.[9] This breakthrough has allowed the exploration of various exciton−photon interaction phenomena, both in the weak[10−17] and strong coupling regimes,[2,18] in the absence of any external microcavity.

However, the removal of external cavities introduces a new challenge regarding the control over the orientation between exciton dipoles and the crystal facets. This angular relationship plays a key role in excitons' interactions with electromagnetic oscillations in their surrounding environment,[19−21] as the coupling strength is governed by a scalar product of the exciton dipole and the photon electric field inside the optical cavity.[22] Traditional molecular crystals allow limited control over molecules' preferred orientation with respect to macroscopic crystalline facets, as the molecular packing motif is determined by weak intermolecular interactions. This heavily restricts chromophore choices for designing exciton−photon interactions,[19] as a large number of polycyclic aromatic hydrocarbons tend to crystallize in herringbone motifs[23] with undesirable tilted dipole arrangements.[21]

Here, we demonstrate that one potential approach to address this challenge is to anchor Frenkel excitons in metal−organic frameworks (MOFs) with directional metal−ligand bonds. This concept is illustrated with a bichromophoric MOF that simultaneously hosts two types of Frenkel excitons, whose transition dipoles are in principle aligned parallel and perpendicular to the widest facets of microplate-shaped
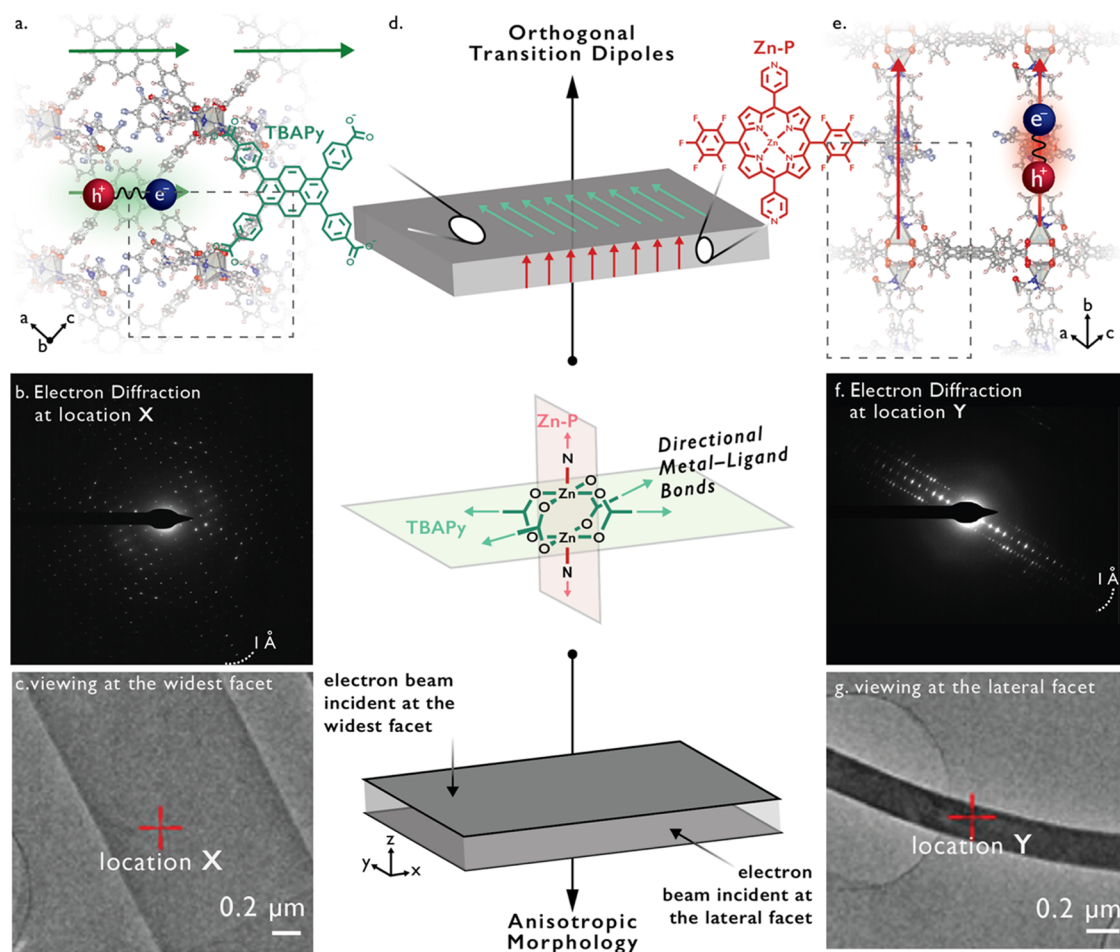
Figure 1. (a) Structure of **PyP-MOF**, viewing from the widest facet of the microplate (dotted box: unit cell). (b) Selected area electron diffraction (SAED) diffractogram and (c) low-magnification cryo-HRTEM micrograph of the widest facet of the **PyP-MOF** microplate. (d) Schematic illustration of the correlation between the molecular axis of the pyrene- and porphyrin-based building blocks and the macroscopic crystalline facets of **PyP-MOF**, which are both influenced by the directional metal–ligand coordination at the $[Zn^{II}]_2$ paddlewheel SBU. Please note that the dipoles are depicted as strictly parallel and perpendicular to the microplate's widest facet for simplicity. In reality, deviation from this ideal relationship can occur due to thermal fluctuation. (e) Structure of **PyP-MOF**, viewing from the lateral facet of the microplate (dotted box: unit cell). (f) SAED diffractogram and (g) low-magnification cryo-HRTEM micrograph of a strip of **PyP-MOF** microplate lying on its lateral facet. The elongation of the diffraction spots results from diffuse scattering caused by the slight bending of this microplate strip. The data presented in (b, c, f, g) are reproduced from our previous work in ref 24 and reproduced with permission from the Royal Society of Chemistry.

crystals. We observe that the orientation of the exciton dipole determines the emission's polarization and impacts whether it is waveguided to the microplates' lateral facets or emitted diffusively.

◼ RESULTS AND DISCUSSION

The bichromophoric MOF ("**PyP-MOF**"), $Zn_2(\textbf{Zn-P})$-(**TBAPy**) (**Zn-P** = [5,15-dipyridyl-10,20-bis (pentafluoro-phenyl)-porphyrinato]-zinc^{II}, $H_4\textbf{TBAPy}$ = pyrene-1,3,6,8-tetrayl-tetrabenzoic acid) anchors two fluorescent ligands at an angle of 90° with respect to each other, enabled by the di-zinc $[Zn_2O_8]$ secondary building unit (SBU). The SBUs connect **TBAPy** tetratopic ligands into rectangular two-dimensional (2D) sheets/layers. Orthogonal to these sheets, ditopic porphyrin-based rod ligands **Zn^{II}-P** connect them into a three-dimensional structure. The tetragonal coordination sphere of the $[Zn_2O_8]$ SBU imposes a perpendicular relationship between the transition dipoles of the pyrene and porphyrin ligands.

Selected area electron diffraction (SAED) targeting the widest and lateral facets of the **PyP-MOF** microplates reveals that the microplates' xy-plane host the pyrene (**TBAPy**) sheets, while the porphyrin pillars lie along the microplates' z-axis (Figure 1d). As reported previously,[24] cryogenic high-resolution transmission electron microscopy (cryo-HRTEM) micrographs capture a rectangular 2D lattice with parameters that match the dimensions of **TBAPy** tetra-coordinated to the zinc SBUs, corroborating the SAED data. Time-dependent density functional theory (TD-DFT) calculations suggest that the transition dipole of the lowest excited singlet state $S_1(\textbf{TBAPy})$ lies within the pyrene ligand's π-plane; while the effective dipole of $S_1(\textbf{Zn-P})$ is along the N–N axis of the porphyrin ligand.[24] Thus, for the specific case of **PyP-MOF**, the transition dipoles of $S_1(\textbf{TBAPy})$ and $S_1(\textbf{Zn-P})$ are aligned parallel and perpendicular to the microplates' widest facet, respectively (Figure 1d).

Variations in macroscopic morphology (size, thickness, and roughness) can be observed among drop-casted **PyP-MOF** microplates. The polydisperse microplates have different contrast on the grayscale of HRTEM micrographs but exhibit

identical SAED patterns, confirming a conserved internal structure. Furthermore, some of the larger microplates that extend over 10 μm also show terraced morphology, with the thickness (and thus the number of layers) varying even within the same crystallite (detailed in the Supporting Information, Section 3.1.3).

The ensemble PL spectrum of bulk **PyP-MOF** solids exhibits two main features with λ_{max} = 503 nm and λ_{max} = 662 nm upon excitation with a 405 nm laser (Figure 2b). Based on comparisons with the PL of the ligand monomers (Figure S3), the higher-energy and lower-energy emissive
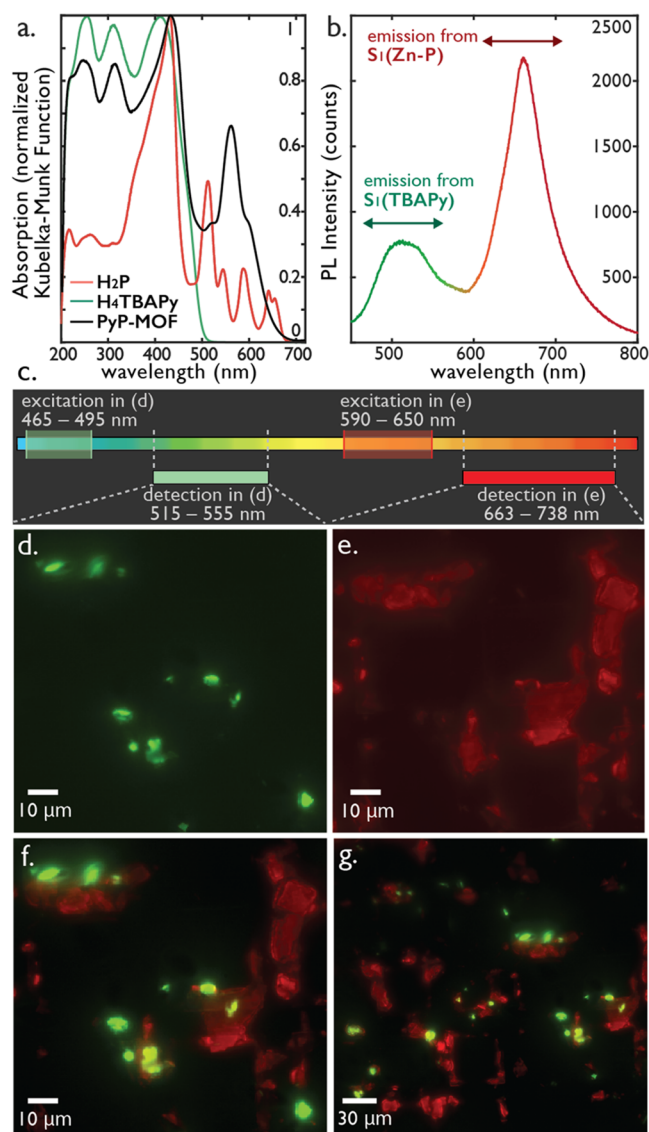
Figure 2. (a) Diffuse reflectance UV−vis absorption spectra of **PyP-MOF** and the ligands (**H$_4$TBAPy** and **H$_2$P**). All samples are measured as solids diluted in KBr. (b) Photoluminescence spectrum of bulk **PyP-MOF** solids (excitation: 405 nm laser). (c) Summary of the excitation and detection windows of the fluorescence micrographs in (d, e). (d) Fluorescence micrograph of neat drop-casted **PyP-MOF** microplates with an excitation window of 465−495 nm and a detection window of 515−555 nm. (e) Fluorescence micrograph of neat drop-casted **PyP-MOF** crystals with an excitation window of 590−650 nm and a detection window of 663−738 nm. (f) Overlay of (d) and (e). (g) Zoomed-out view of (f) capturing a larger field of view.

states of **PyP-MOF** are assignable to S$_1$(**TBAPy**) and S$_1$(**Zn-P**), respectively. The dual-band emission in this material is enabled by an inhibited Förster resonance energy transfer (from pyrene to porphyrin) due to the perpendicular arrangement of the dipoles of the pyrene and the porphyrin moieties, as detailed in our previous work.[24]

At the single-particle level, fluorescence microscopy reveals a striking difference between the spatial distributions of the emissions from S$_1$(**TBAPy**) and S$_1$(**Zn-P**). The fluorescence micrographs in Figure 2d,e are measured on the exact same region of drop-casted **PyP-MOF** microplates, with excitation/emission windows to capture PL from S$_1$(**TBAPy**) and S$_1$(**Zn-P**), respectively. Comparison of (d, e) and their overlapped views (f, g) shows that S$_1$(**TBAPy**) PL is emitted dominantly from the lateral facets of the microplates, while the S$_1$(**Zn-P**) emission is more diffusively distributed across all facets of the microplates.

Confocal laser scanning microscopy resolved finer spatial details of the anomalous waveguiding effect in **PyP-MOF** microplates. A focused 405 nm laser spot was scanned across a TEM grid with neat drop-casted **PyP-MOF** microplates. The fluorescence intensity from each laser-excited spot on the microplate was recorded one pixel at a time (pixel size = 0.132 μm × 0.132 μm), allowing a high level of spatial resolution in the xy-plane. Meanwhile, resolution in the z-dimension is enhanced by suppression of light originating from outside of the desired focal plane.

To isolate emissions originating from S$_1$(**TBAPy**) and S$_1$(**Zn-P**), two photomultiplier tube (PMT) detectors were coupled with bandpass filters of 452−578 nm and 651−754 nm. These two detectors separately capture emissions from the pyrene and porphyrin singlet states and are labeled as Channel 1 (Ch1, green) and Chanel 2 (Ch2, red), respectively. In addition, transmission micrographs are recorded and overlaid with fluorescence micrographs to locate non-emissive locations. As shown in Figure 3b,d, the fluorescence intensity of S$_1$(**TBAPy**) varies sharply within each microplate. In contrast, the emission profile of S$_1$(**Zn-P**) is relatively uniform across each microplate (Figure 3c,e).

Targeting further spectral details, we complemented the 2-channel detection setup with a "λ-scan" setup (Figure 3h) that collects emissions from 417 to 717 nm at a step size of 5 nm. To extract region-specific spectral profile, we measured the average fluorescence intensities of the same selected subregions for all 60 λ-frames and plotted these values against the corresponding wavelength. This analysis was repeated and averaged over four random locations for both lateral and the widest facets of the microplate. As shown in Figure 3i, the averaged spectrum of the lateral facets is dominated by an intense waveguided S$_1$(**TBAPy**) spanning from 450 to 550 nm (λ_{max} ~475 nm). It also contains a shoulder from S$_1$(**Zn-P**) spanning from 550 to 700 nm (λ_{max} ~650 nm). On the other hand, the PL from the widest facet (Figure 3j) comprises a single feature (λ_{max} ~660 nm) assignable to emission from S$_1$(**Zn-P**). These λ-scan measurements corroborate the distinct spatial and spectral profiles of the S$_1$(**TBAPy**) and S$_1$(**Zn-P**) emission bands that coexist in **PyP-MOF**.

The localization of pyrene emission at the microplates' lateral facets is characteristic of the behavior of "active waveguides"—materials that propagate their intrinsic photoluminescence toward crystals' terminals.[13,16,25−36] In contrast to passive waveguides that only reflect/refract photons, active waveguides also absorb photons, leading to exciton formation.
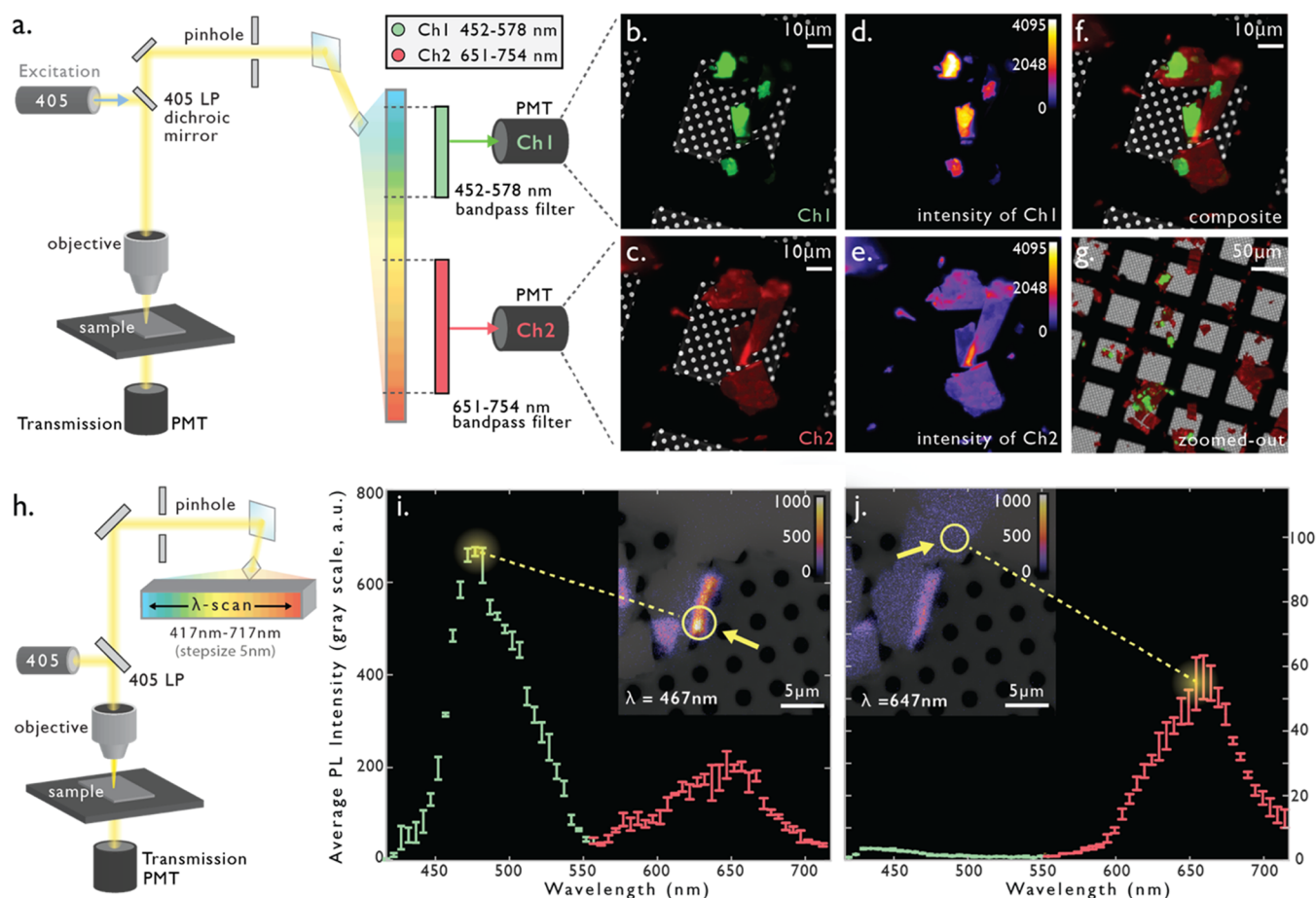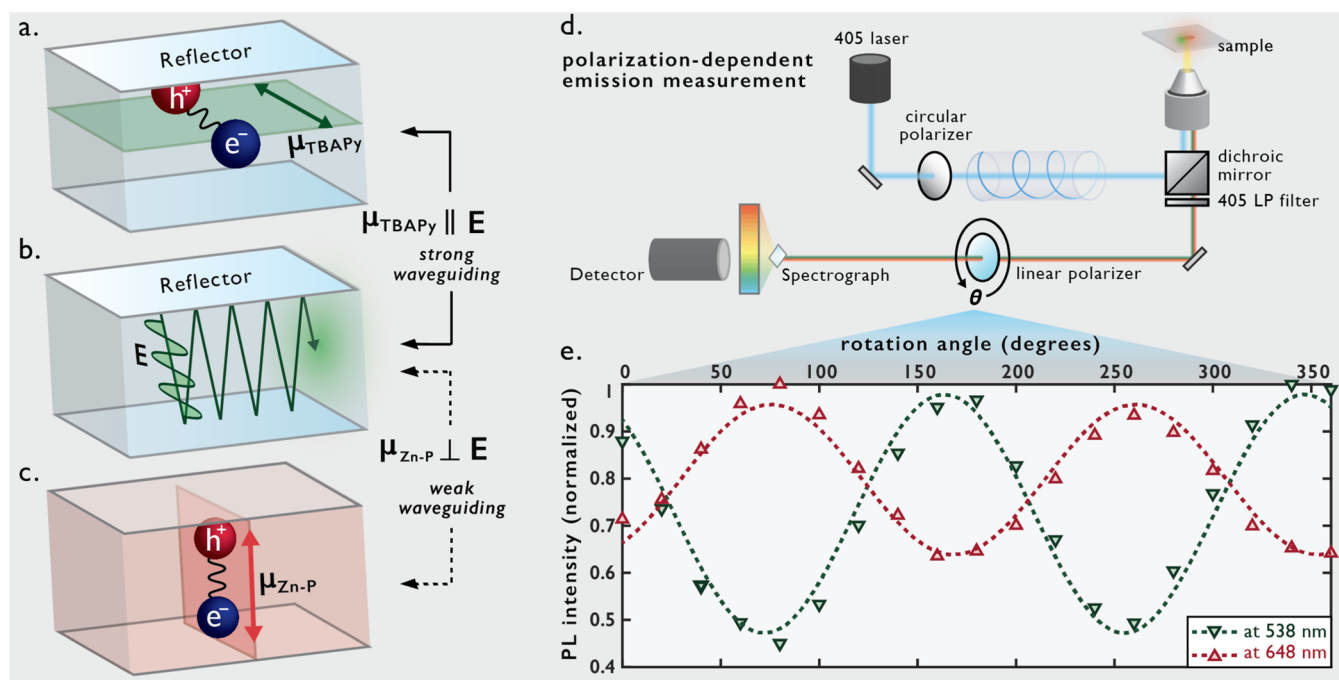
Figure 3. (a) Schematic illustration of the setup of laser scanning confocal microscopy with 2-channel detection. Channel 1 (Ch1) and Channel 2 (Ch2) collect emissions in the ranges of 452−578 and 651−754 nm, respectively. (b, c) Fluorescence micrographs of neat **PyP-MOF** microplates drop-casted on a TEM grid captured in Ch1 (colored green) and Ch2 (colored red), respectively. (d, e) Intensity profiles of the fluorescence micrographs captured in Ch1 and Ch2. (f, g) Fluorescence micrographs showing overlays of the two channels. (h) Schematic illustration of the setup of spectrally resolved laser scanning confocal microscopy (λ-scan). (i) Region-specific PL spectrum extracted from the lateral facet where waveguided pyrene emission is observed (region circled in the inset). Inset: example of a single λ-scan frame (467−472 nm) of laser scanning confocal microscopy. (j) Region-specific PL spectrum extracted from the widest facet where porphyrin emission is observed (region circled in the inset). Inset: example of a single λ-scan frame (647−652 nm) of laser scanning confocal microscopy.

Since both forms of oscillations (exciton + photon) contribute to the energy flow in these systems,[4,20] the relative orientation between the exciton dipole and the microcavity is a critical variable that impacts the waveguiding behavior.[37] Through cyro-HRTEM/SAED characterization (Figure 1b,f), we demonstrated that the dipoles of S_1(**TBAPy**) and S_1(**Zn-P**) feature distinct orientations with respect to the microplate facets, leading to different levels of coupling to the photon electric field in the microcavity (Figure 4a−c). Thus, we hypothesize that the distinct degrees of waveguiding observed for the two emission bands can be attributed to **PyP-MOF**'s anisotropic structure, which translates into an anisotropic dielectric function within this system.

To test our hypothesis, we probed the polarization of the **PyP-MOF** emission from a single microplate by placing a linear polarizer in the PL detection optical pathway (Figure 4d and Supporting Information, Section 2.3). Upon rotating the polarizer from 0 to 360° at a step size of 20°, the intensities of emission bands at 450−600 nm and 600−750 nm showed opposite changes (Figures 4e and S2). The correlation between the maxima and the minima of S_1(**TBAPy**) and S_1(**Zn-P**) PL indicates that the exciton/photon fields of the

two emission bands are orthogonally polarized within the microresonator.

It is worth noting that the confinement of waveguided photons is highly sensitive to the crystal's macroscopic morphology. As briefly discussed earlier, some **PyP-MOF** microplates, especially those larger than 10 μm, bear imperfections and have non-uniform thickness. The variation of the thickness both among different microplates and within the same microplate can result in regions where the waveguiding of the pyrene PL is no longer supported. This explains the variation in the degree of pyrene emission waveguiding that can be detected upon surveying a large number of **PyP-MOF** crystals. Specifically, in addition to the microplates that glow intensely green only from their lateral facet, two types of outliers are found: (i) large microplate aggregates where patches of their widest facet show weak pyrene emission and (ii) extremely thin microplates that emit green from all facets. In both cases, the pyrene emission is much weaker in intensity than the waveguided pyrene emission from the lateral facets. This weaker emission is attributed to a combination of scattering from crystal surface imperfections

Figure 4. (a−c) Schematic illustration of the parallel and perpendicular arrangement of the pyrene and porphyrin singlet exciton dipole with respect to the waveguided photon electric field. (d) The experimental setup for the measurement of the polarization-dependent PL from a single **PyP-MOF** microplate. (e) The polarization-dependent intensities of PL at 538 and 648 nm, which are derived from S_1(**TBAPy**) and S_1(**Zn-P**), respectively. Dotted line: sinusoidal fitting of the experimental data.

and thickness/dielectric contrast variations that diminish the strength of the waveguiding effect.

In addition to the orthogonal polarization, the pyrene- and the porphyrin-based PL also feature opposite changes in intensity upon cooling to 77 K. The temperature-dependent fluorescence microscopy was carried out by coupling the spectrally resolved setup (Figure 3h) with a liquid nitrogen-cooled cryostage (Figure S1). As shown in Figure 5a, the intensity of the waveguided pyrene emission (450−550 nm) spiked upon cooling to 77 K, reaching approximately 3 times its room temperature value. In contrast, the intensity of the porphyrin emission (600−700 nm) was quenched upon cooling (Figure 5b). In addition, the weak non-waveguided pyrene emission also showed a decreased intensity at 77 K (Figure 5c,d)

Several factors can contribute to the opposite temperature dependence observed for the waveguided and the non-waveguided PL intensities. Upon cooling, the pyrene excitons' interaction with the waveguided photon can become more favorable due to less thermal broadening of the emission line width, thereby giving rise to the simultaneous increase of waveguided pyrene PL intensity and decrease of non-waveguided pyrene PL intensity. Other factors that can lead to the spike of waveguided pyrene PL at 77 K include reduced non-radiative decay and reduced re-absorption at lower temperatures. On the other hand, the quenching of the porphyrin singlet emission at 77 K can result from the reduced thermal fluctuation upon cooling, which imposes a more rigid perpendicular arrangement of the two chromophores' dipoles and a stronger inhibition of the S_1(**TBAPy**) → S_1(**Zn-P**) energy transfer.[24]
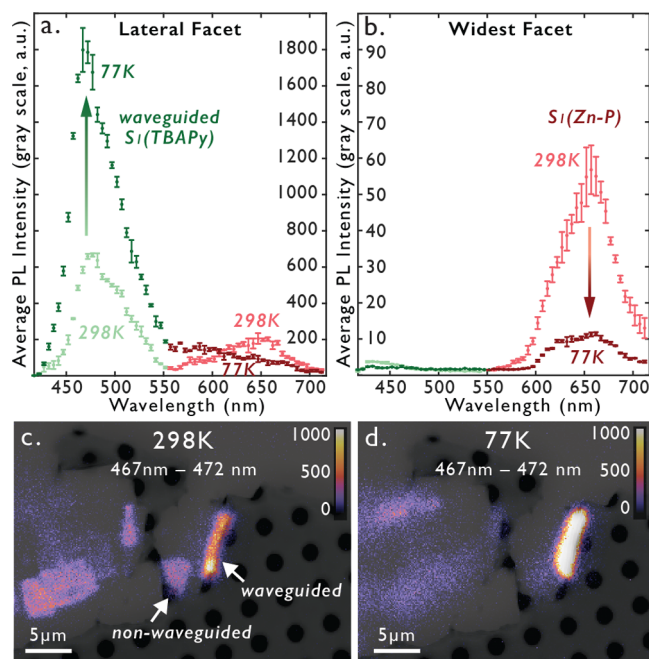
Figure 5. (a, b) Temperature-dependent intensities of PL from the **PyP-MOF** microplate's lateral and widest facets, which are dominated by the waveguided S_1(**TBAPy**) emission and the S_1(**Zn-P**) emission, respectively. (c) Room-temperature fluorescence micrograph at a wavelength segment of 467−472 nm (overlapped with the transmission micrograph). (d) 77 K fluorescence micrograph at a wavelength segment of 467−472 nm (overlapped with the transmission micrograph).

■ CONCLUSIONS

In conclusion, we observed that perpendicularly oriented **TBAPy** and **Zn-P** ligands in a single **PyP-MOF** microplate can

simultaneously fluorescence with distinct spatial distribution, orthogonal polarization, and opposite temperature dependence. Laser scanning fluorescence microscopy reveals that emission from $S_1(\textbf{TBAPy})$ is waveguided toward the lateral facets of the microplates, while $S_1(\textbf{Zn-P})$ emits diffusively. This dipole-dependent waveguide effect signals a highly anisotropic dielectric function of **PyP-MOF**, which is further evidenced by the orthogonal polarizations of the two emission bands. Using this system, we highlight that directional metal−ligand interactions in MOFs can be leveraged to orient exciton dipoles and photon electric fields in a crystal-based microcavity. These observations point toward MOFs' potential application in the growing field of exciton−photonics, where the coupling between excitons and photons lies at the center of next-generation optoelectronic technologies ranging from photonic circuits to polaritonic devices.[19]

■ ASSOCIATED CONTENT

ⓈⒾ Supporting Information

The Supporting Information is available free of charge at https://pubs.acs.org/doi/10.1021/jacs.3c06678.

> Full descriptions of the experimental methods and supplementary photophysical/structural data (PDF)

■ AUTHOR INFORMATION

Corresponding Authors

William A. Tisdale − *Department of Chemical Engineering, Massachusetts Institute of Technology, Cambridge, Massachusetts 02139, United States;* Ⓞ orcid.org/0000-0002-6615-5342; Email: tisdale@mit.edu

Mircea Dincă − *Department of Chemistry, Massachusetts Institute of Technology, Cambridge, Massachusetts 02139, United States;* Ⓞ orcid.org/0000-0002-1262-1264; Email: mdinca@mit.edu

Authors

Ruomeng Wan − *Department of Chemistry, Massachusetts Institute of Technology, Cambridge, Massachusetts 02139, United States;* Ⓞ orcid.org/0000-0001-8824-7128

David Mankus − *David H. Koch Institute for Integrative Cancer Research, Massachusetts Institute of Technology, Cambridge, Massachusetts 02139, United States;* Ⓞ orcid.org/0000-0002-9979-7608

Woo Seok Lee − *Department of Chemical Engineering and Department of Materials Science and Engineering, Massachusetts Institute of Technology, Cambridge, Massachusetts 02139, United States;* Ⓞ orcid.org/0000-0001-9188-5104

Abigail K. R. Lytton-Jean − *David H. Koch Institute for Integrative Cancer Research, Massachusetts Institute of Technology, Cambridge, Massachusetts 02139, United States*

Complete contact information is available at:
https://pubs.acs.org/10.1021/jacs.3c06678

Author Contributions

⊥D.M. and W.S.L. contributed equally to this paper.

Notes

The authors declare no competing financial interest.

■ ACKNOWLEDGMENTS

■ REFERENCES

(1) Schouwink, P.; Berlepsch, H. V.; Dähne, L.; Mahrt, R. F. Observation of Strong Exciton−Photon Coupling in an Organic Microcavity. *Chem. Phys. Lett.* **2001**, *344*, 352−356.

(2) Tang, J.; Zhang, J.; Lv, Y.; Wang, H.; Xu, F. F.; Zhang, C.; Sun, L.; Yao, J.; Zhao, Y. S. Room Temperature Exciton−Polariton Bose−Einstein Condensation in Organic Single-Crystal Microribbon Cavities. *Nat. Commun.* **2021**, *12*, No. 3265.

(3) Takazawa, K.; Inoue, J.; Mitsuishi, K.; Takamasu, T. Fraction of a Millimeter Propagation of Exciton Polaritons in Photoexcited Nanofibers of Organic Dye. *Phys. Rev. Lett.* **2010**, *105*, No. 067401.

(4) Kéna-Cohen, S.; Davanço, M.; Forrest, S. R. Strong Exciton-Photon Coupling in an Organic Single Crystal Microcavity. *Phys. Rev. Lett.* **2008**, *101*, No. 116401.

(5) Cookson, T.; Georgiou, K.; Zasedatelev, A.; Grant, R. T.; Virgili, T.; Cavazzini, M.; Galeotti, F.; Clark, C.; Berloff, N. G.; Lidzey, D. G.; Lagoudakis, P. G. A Yellow Polariton Condensate in a Dye Filled Microcavity. *Adv. Opt. Mater.* **2017**, *5*, No. 1700203.

(6) Kéna-Cohen, S.; Forrest, S. R. Room-Temperature Polariton Lasing in an Organic Single-Crystal Microcavity. *Nat. Photonics* **2010**, *4*, 371−375.

(7) Daskalakis, K. S.; Maier, S. A.; Murray, R.; Kéna-Cohen, S. Nonlinear Interactions in an Organic Polariton Condensate. *Nat. Mater.* **2014**, *13*, 271−278.

(8) Tischler, J. R.; Bradley, M. S.; Bulović, V.; Song, J. H.; Nurmikko, A. Strong Coupling in a Microcavity LED. *Phys. Rev. Lett.* **2005**, *95*, No. 036401.

(9) Meskers, S. C. J.; Lakhwani, G. Reflection of Light by Anisotropic Molecular Crystals Including Exciton-Polaritons and Spatial Dispersion. *J. Chem. Phys.* **2016**, *145*, No. 194703.

(10) Zhang, C.; Zou, C.-L.; Dong, H.; Yan, Y.; Yao, J.; Zhao, Y. S. Dual-Color Single-Mode Lasing in Axially Coupled Organic Nanowire Resonators. *Sci. Adv.* **2017**, *3*, No. e1700225.

(11) Takazawa, K.; Inoue, J.; Mitsuishi, K.; Takamasu, T. Micrometer-Scale Photonic Circuit Components Based on Propagation of Exciton Polaritons in Organic Dye Nanofibers. *Adv. Mater.* **2011**, *23*, 3659−3663.

(12) Annadhasan, M.; Vinod Kumar, A.; Giri, P.; Nandy, S.; Panda, M. K.; Jovan Jose, K. V.; Chandrasekar, R. Dimension Engineering of Stimuli-Responsive 1D Molecular Crystals into Unusual 2D and 3D Zigzag Waveguides. *Angew. Chem., Int. Ed.* **2023**, *62*, No. e202302929.

(13) Wu, S.; Zhou, B.; Yan, D. Recent Advances on Molecular Crystalline Luminescent Materials for Optical Waveguides. *Adv. Opt. Mater.* **2021**, *9*, No. 2001768.

(14) Catalano, L.; Berthaud, J.; Dushaq, G.; Karothu, D. P.; Rezgui, R.; Rasras, M.; Ferlay, S.; Hosseini, M. W.; Naumov, P. Sequencing and Welding of Molecular Single-Crystal Optical Waveguides. *Adv. Funct. Mater.* **2020**, *30*, No. 2003443.

(15) Feiler, T.; Bhattacharya, B.; L Michalchuk, A. A.; Rhim, S.-Y.; Schröder, V.; List-Kratochvil, E.; Emmerling, F. Tuning the Mechanical Flexibility of Organic Molecular Crystals by Polymorphism for Flexible Optical Waveguides. *CrystEngComm* **2021**, *23*, 5815−5825.

(16) Catalano, L.; Karothu, D. P.; Schramm, S.; Ahmed, E.; Rezgui, R.; Barber, T. J.; Famulari, A.; Naumov, P. Dual-Mode Light Transduction through a Plastically Bendable Organic Crystal as an Optical Waveguide. *Angew. Chem., Int. Ed.* **2018**, *57*, 17254−17258.

(17) Matsuo, T.; Ikeda, K.; Hayashi, S. Flexible Förster Resonance Energy Transfer-Assisted Optical Waveguide Based on Elastic Mixed Molecular Crystals *Aggregate* e378 DOI: 10.1002/agt2.378.

(18) Cui, Q. H.; Peng, Q.; Luo, Y.; Jiang, Y.; Yan, Y.; Wei, C.; Shuai, Z.; Sun, C.; Yao, J.; Zhao, Y. S. Asymmetric Photon Transport in Organic Semiconductor Nanowires through Electrically Controlled Exciton Diffusion. *Sci. Adv.* **2018**, *4*, No. eaap9861.

(19) Anantharaman, S. B.; Jo, K.; Jariwala, D. Exciton−Photonics: From Fundamental Science to Applications. *ACS Nano* **2021**, *15*, 12628−12654.

(20) Li, Y. J.; Hong, Y.; Peng, Q.; Yao, J.; Zhao, Y. S. Orientation-Dependent Exciton−Plasmon Coupling in Embedded Organic/Metal Nanowire Heterostructures. *ACS Nano* **2017**, *11*, 10106−10112.

(21) Goto, K.; Yamashita, K.; Yanagi, H.; Yamao, T.; Hotta, S. Strong Exciton-Photon Coupling in Organic Single Crystal Microcavity with High Molecular Orientation. *Appl. Phys. Lett.* **2016**, *109*, No. 061101.

(22) Hertzog, M.; Wang, M.; Mony, J.; Börjesson, K. Strong Light−Matter Interactions: A New Direction within Chemistry. *Chem. Soc. Rev.* **2019**, *48*, 937−961.

(23) Campbell, J. E.; Yang, J.; Day, G. Predicted Energy−Structure−Function Maps for the Evaluation of Small Molecule Organic Semiconductors. *J. Mater. Chem. C* **2017**, *5*, 7574−7584.

(24) Wan, R.; Ha, D.-G.; Dou, J.-H.; Lee, W. S.; Chen, T.; Oppenheim, J. J.; Li, J.; Tisdale, W. A.; Dincă, M. Dipole-Mediated Exciton Management Strategy Enabled by Reticular Chemistry. *Chem. Sci.* **2022**, *13*, 10792−10797.

(25) Liu, H.; Lu, Z.; Zhang, Z.; Wang, Y.; Zhang, H. Highly Elastic Organic Crystals for Flexible Optical Waveguides. *Angew. Chem., Int. Ed.* **2018**, *57*, 8448−8452.

(26) Huang, R.; Wang, C.; Wang, Y.; Zhang, H. Elastic Self-Doping Organic Single Crystals Exhibiting Flexible Optical Waveguide and Amplified Spontaneous Emission. *Adv. Mater.* **2018**, *30*, No. 1800814.

(27) Annadhasan, M.; Karothu, D. P.; Chinnasamy, R.; Catalano, L.; Ahmed, E.; Ghosh, S.; Naumov, P.; Chandrasekar, R. Micromanipulation of Mechanically Compliant Organic Single-Crystal Optical Microwaveguides. *Angew. Chem.* **2020**, *132*, 13925−13934.

(28) Huang, R.; Tang, B.; Ye, K.; Wang, C.; Zhang, H. Flexible Luminescent Organic Bulk Crystal: 2D Elasticity toward 3D Optical Waveguide. *Adv. Opt. Mater.* **2019**, *7*, No. 1900927.

(29) Hayashi, S.; Yamamoto, S.; Takeuchi, D.; Ie, Y.; Takagi, K. Creating Elastic Organic Crystals of π-Conjugated Molecules with Bending Mechanofluorochromism and Flexible Optical Waveguide. *Angew. Chem., Int. Ed.* **2018**, *57*, 17002−17008.

(30) Liu, B.; Di, Q.; Liu, W.; Wang, C.; Wang, Y.; Zhang, H. Red-Emissive Organic Crystals of a Single-Benzene Molecule: Elastically Bendable and Flexible Optical Waveguide. *J. Phys. Chem. Lett.* **2019**, *10*, 1437−1442.

(31) Lu, Z.; Zhang, Y.; Liu, H.; Ye, K.; Liu, W.; Zhang, H. Optical Waveguiding Organic Single Crystals Exhibiting Physical and Chemical Bending Features. *Angew. Chem., Int. Ed.* **2020**, *59*, 4299−4303.

(32) Annadhasan, M.; Agrawal, A. R.; Bhunia, S.; Pradeep, V. V.; Zade, S. S.; Reddy, C. M.; Chandrasekar, R. Mechanophotonics: Flexible Single-Crystal Organic Waveguides and Circuits. *Angew. Chem.* **2020**, *132*, 13956−13962.

(33) Liu, H.; Lu, Z.; Tang, B.; Qu, C.; Zhang, Z.; Zhang, H. A Flexible Organic Single Crystal with Plastic-Twisting and Elastic-Bending Capabilities and Polarization-Rotation Function. *Angew. Chem.* **2020**, *132*, 13044−13050.

(34) Zhao, G.; Dong, H.; Liao, Q.; Jiang, J.; Luo, Y.; Fu, H.; Hu, W. Organic Field-Effect Optical Waveguides. *Nat. Commun.* **2018**, *9*, No. 4790.

(35) Liu, H.; Bian, Z.; Cheng, Q.; Lan, L.; Wang, Y.; Zhang, H. Controllably Realizing Elastic/Plastic Bending Based on a Room-Temperature Phosphorescent Waveguiding Organic Crystal. *Chem. Sci.* **2019**, *10*, 227−232.

(36) Annadhasan, M.; Basak, S.; Chandrasekhar, N.; Chandrasekar, R. Next-Generation Organic Photonics: The Emergence of Flexible Crystal Optical Waveguides. *Adv. Opt. Mater.* **2020**, *8*, No. 2000959.

(37) Liu, Y.; Hu, H.; Xu, L.; Qiu, B.; Liang, J.; Ding, F.; Wang, K.; Chu, M.; Zhang, W.; Ma, M.; Chen, B.; Yang, X.; Zhao, Y. S. Orientation-Controlled 2D Anisotropic and Isotropic Photon Transport in Co-Crystal Polymorph Microplates. *Angew. Chem., Int. Ed.* **2020**, *59*, 4456−4463.

G